Available online at www.sciencedirect.com
ScienceDirect
Tectonophysics 432 (2007) 1 – 19
TECTONOPHYSICS
www.elsevier.com/locate/tecto

Local tomography and focal mechanisms in the south-western Alps: Comparison of methods and tectonic implications

Béthoux Nicole [a,*], Sue Christian [b,1], Paul Anne [b], Virieux Jean [a], Fréchet Julien [b], Thouvenot François [c], Cattaneo Marco [c]

[a] Géosciences Azur, Université de Nice et CNRS, 250 rue Albert Einstein, 06560 Valbonne, France
[b] Laboratoire de Géophysique Interne et Tectonophysique, Observatoire de Grenoble, CNRS et Université Joseph Fourier, BP 53, 38051 Grenoble Cedex 9, France (now at EOPGS, 5, rue René Descartes, 67084 Strasbourg Cedex, France)
[c] Dipartimento Scienze della Terra, Universita di Genova, Viale Benedetto XV, 5,1632 Genova, Italy (now at INGV, Via Di Vigna Murato, 00143 Roma, Italy)

Received 24 March 2006; received in revised form 28 September 2006; accepted 5 October 2006
Available online 19 January 2007

Abstract

We investigate how focal solutions and hypocenter locations may depend on the ray tracing algorithm and the strategy of velocity inversion. Using arrival times from a temporary seismological network in the south-western Alps, a local earthquake tomography has been performed by Paul et al. [Paul, A., Cattaneo, M., Thouvenot, F., Spallarossa, D., Béthoux, N., and Fréchet, J., 2001. A three-dimensional crustal velocity model of the south-western Alps from local earthquake tomography. J. Geophys. Res. 106, 19367–19390.] with the method developed by Thurber [Thurber, C.H., 1993. Local earthquake tomography: velocity and Vp/Vs-Theory, in Seismic Tomography: Theory and practice, Iyer, H.M., and Irahara eds., Chapman and Hall, New York, 563–583.]. Another inversion of the same data set is performed here using a different tomography code relying on a shooting paraxial method and cubic interpolation of velocities. The resulting images display the same main features, although Thurber's code appears to be more robust in regions with scarce ray coverage and strong velocity contrasts. Concerning hypocenter location in Piemont units, one major result is the concentration of hypocenters at the boundary between the mantle wedge of the Ivrea body and the European crust. Forty-six focal mechanisms are shown that were computed using both the take-off angles in the minimum 1-D model and in the 3-D velocity structures resulting from the two inversions. The sets of focal solutions are very similar, proving the reliability and the coherency of the focal solutions. The widespread extension in the core of the western Alps is confirmed whereas a few compressive solutions are found east of the Piemont units. These results constrain the sharp change of stress tensor and evidence a decoupling of strain beneath the east of Dora Maira massif up to beneath the north of Argentera massif. On a geodynamical point of view seismicity and focal mechanism distribution are compatible with the present day models published for the western Alps, where the major feature is the lithospheric thickening [Schmid, S.M., and Kissling, E., 2000. The arc of the western Alps in the light of geophysical data on deep crustal structure. Tectonics, 19, 62–85.], implying widespread extension in the core of the western Alps [Sue, C., Thouvenot, F., Fréchet, J., and Tricart, P., 1999. Widespread extension in the core of the western Alps revealed by earthquake analysis. J. Geophys. Res., 104, 25611–25622.]. However the existence of compressive events dealing at depth with the boundary of Ivrea body allows to postulate that this

* Corresponding author.
E-mail address: nbethoux@obs-vlfr.fr (B. Nicole).
[1] Present address: Université de Bretagne Occidentale, UMR 6338, Place Nicolas Copernic, 29280 Plouzané, France.

doi:10.1016/j.tecto.2006.10.004

geological structure is still tectonically active. Even if field work has not shown this so far, the Insubric line appears to extend toward the south at depth, as a blind fault, and to play a key role in the dynamics of the south-western Alps.

Keywords: Western Alps; Crust; Local earthquake tomography; Focal mechanisms; Seismicity; Tectonics

1. Introduction

It is well known that fault plane solutions of local earthquakes based on P-wave first motions strongly depend on correct identification of phase arrivals and on reliable estimates of the take-off angle of the rays at the source. This sensitivity is particularly important for shallow earthquakes located in regions with strong crustal heterogeneity. The first goal of this study was to test the reliability of 1-D focal solutions compared to solutions in a highly heterogeneous three-dimensional medium. However, the studied area is a key example to compare crustal velocity models obtained with two different local earthquake tomography (LET) codes because very strong velocity contrasts have been observed in the crust (Paul et al., 2001). Thus we also tested the influence of the resulting 3-D velocity structures on the hypocenter locations and focal mechanisms. This work demonstrates that improved earthquake locations and focal solutions computed in a 3-D velocity model lead to a more precise seismotectonic analysis of this tectonically and structurally very complex part of the Alpine domain.

This study was part of the GéoFrance 3-D project (Groupe de recherche Géofrance 3-D, 1997) launched in 1996 to improve our understanding of the recent to present dynamics of the south-western Alps with respect to its three-dimensional structure. The selected area is the southwest termination of the Alpine arc (Fig. 1), a fully three-dimensional target where contradictory kinematic models have been proposed (Laubscher, 1971; Tapponnier, 1977; Vialon et al., 1989). It is also one of the most seismically active areas of Western Europe and its deep structure is largely unknown.

A temporary network of 67 seismological stations was installed between August and December 1996 to complement the 59 permanent stations of the Grenoble, Genova and Nice universities, decreasing the inter-station distance to 10–15 km (Fig. 1). This dense network provided high quality records of more than 1000 local earthquakes. From this database, we computed 46 well-constrained focal solutions using the so-called “minimum 1-D velocity model” computed by Paul et al. (2001) following a procedure similar to the one described in Kissling et al. (1994). Paul et al. (2001) performed a LET using the classical method of Thurber (1983) and Eberhart-Phillips (1993). 347 events were selected from the database and complemented with 99 deep-focus earthquakes located beneath the Po plain and recorded by the permanent network of the Genova University, and 104 quarry blasts. The results of this study including the resolution analysis are presented in Paul et al. (2001) and we shall briefly recall its main conclusions. The LET enhances the strong heterogeneity of the crustal structure. Indeed, this region is characterized by shallow low velocity in the western part of the area, corresponding to the Alpine nappes of the Digne region, and very high velocities at depths larger than 8 km in the easternmost part, corresponding to the so-called Ivrea body. This body has been interpreted as a mantle slice wedged into the European crust (Thouvenot, 1996; Schmid and Kissling, 2000). In such a heterogeneous medium, ray paths strongly depart from those computed in a 1-D medium.

We firstly compare event locations, take-off angles and focal solutions computed in the minimum 1-D velocity model to those of the 3-D velocity model computed by Paul et al. (2001) using the SIMULPS code (Thurber, 1983; Eberhart-Phillips, 1993). Secondly, starting from the same data set and 1-D initial model, we perform another LET using the TOMORAY code described in Virieux (1991), and already applied to the Corinthe (Le Meur et al., 1997) and Garm regions (Ghose et al., 1998). We then compare the 3-D velocity structures, event locations and focal solutions obtained with the two codes.

2. Comparison of the results of SIMULPS and TOMORAY

SIMULPS is an iterative inversion code of local earthquake arrival times for 3-D velocity structure and hypocenter parameters (Thurber, 1983; Eberhart-Phillips, 1993; Thurber, 1993). The 3-D-velocity model is defined at a grid of nodes which can be unevenly spaced, and velocity at any point is obtained by linear interpolation between the 8 neighboring grid nodes. Rays are traced in a two-step approach. The first step is an approximate ray tracing which calculates circular arc ray paths with varying circle radii. The path with the shortest

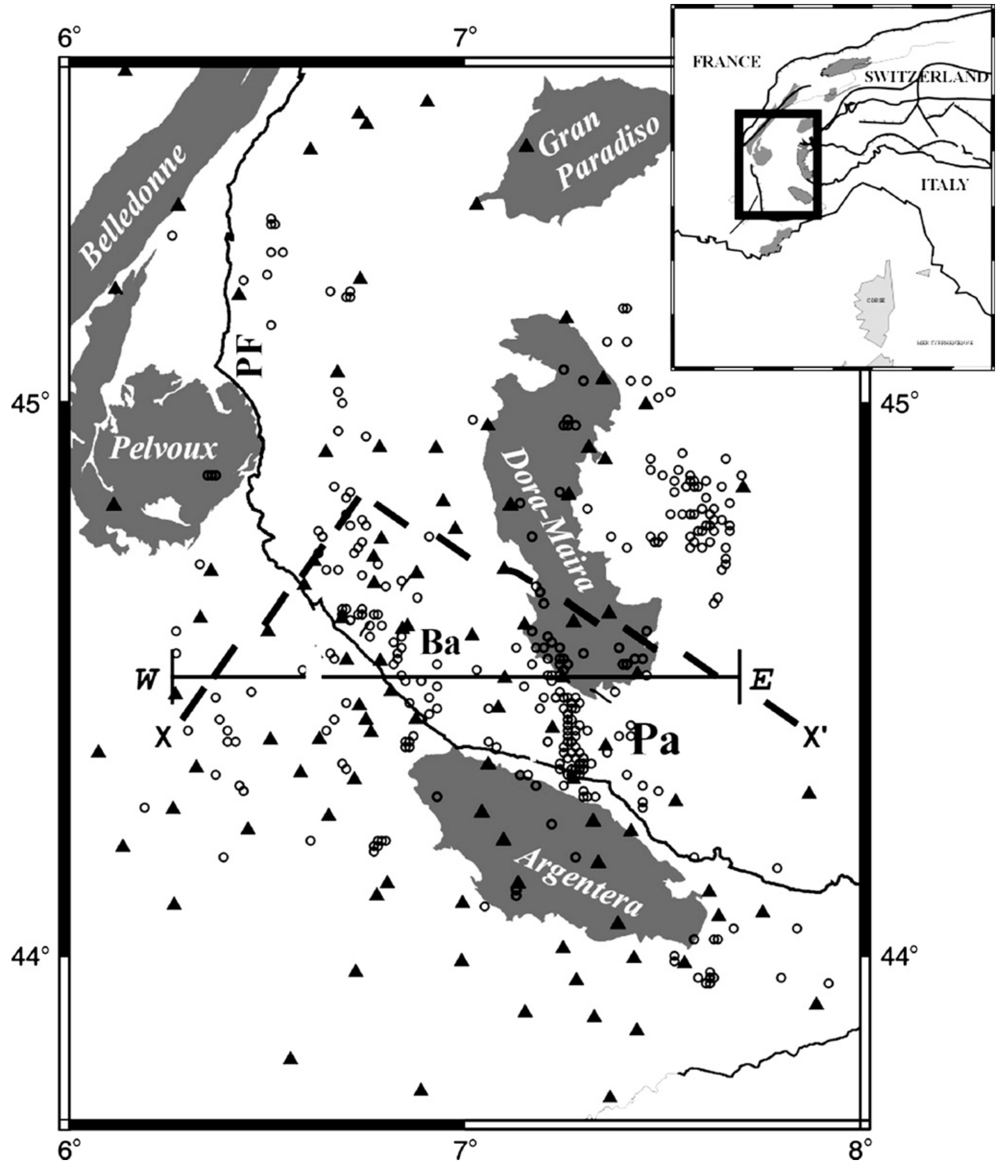

Fig. 1. Location map of stations and epicenters used in this study. Stations are plotted as black triangles and epicenters as dots. The crystalline massifs are filled with grey pattern. PF: Penninic front, B: Briançonnais arc, P: Piemont arc. The location of the depth cross-section of Fig. 13 is plotted as a line, denoted W–E. The location of the geological interpretative cross-section of Fig. 14 is plotted as a dashed line X–X′.

travel time is then perturbed by pseudo-bending (Um and Thurber, 1987), where ray points are moved to locally minimize the travel time on each ray segment. The optimization method used is the Levenberg–Marquardt damped iterative least square inversion (Thurber, 1983).

In the TOMORAY code (Virieux, 1991) the initial velocity model is transformed into squared slowness, which is the output parameter of the inversion (for more details, see Le Meur et al., 1997). So far, the medium can only be discretized on a regular grid. The shooting paraxial method (Virieux et al., 1988) solves the ray equation in a smooth medium obtained by cubic interpolation of slowness. The LSQR method (Paige and Saunders, 1982) is used to solve the inverse problem. SIMULPS inverts for the Vp/Vs ratio, whereas S-wave velocities are inverted independently from P-wave velocities in TOMORAY. Therefore the two codes rely on different ray tracing schemes, different discretizations of the 3-D velocity medium and different inversion techniques.

Haslinger and Kissling (2001) compared the two ray tracing techniques, introducing the shooting ray tracing method in the SIMULPS code. From the analysis of ray

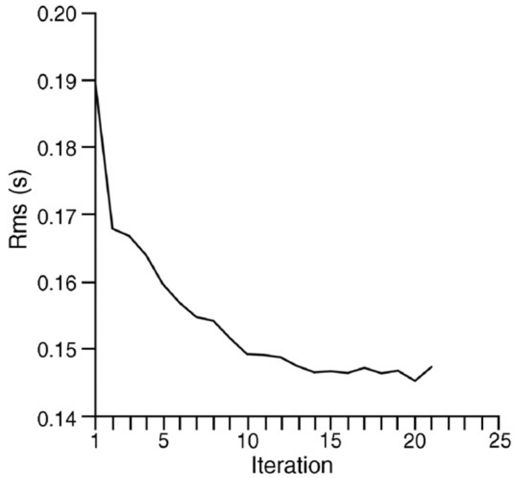

Fig. 2. Decrease of the Rms of both P and S arrival times for an increasing number of TOMORAY iterations of simultaneous inversion for velocity and earthquake parameters.

paths in a synthetic 3-D medium, they concluded that for ray lengths shorter than 60 km, the travel times computed with the two ray tracers are identical with respect to the size of the Fresnel zone. For longer distances, the shooting method provides more accurate results in the absence of strong velocity contrast. In case of strong heterogeneity, paraxial rays cannot be computed whereas pseudo-bending rays are approximate but more robust. These two versions of SIMULPS have also been used in northwestern Greece, and no significant difference in the resulting velocity models has been observed (Haslinger et al., 1999).

In this study, we compare not only the ray tracing technique but the whole LET process, including modeling of the velocity structure and inversion techniques. Our data involve a wider area (160 * 160 km) and stronger velocity changes (>15%) than in the previous study by Haslinger and Kissling (2001).

2.1. Parameterization and resolution tests

The first LET by Paul et al. (2001) was achieved with a grid spacing of 10 km in the horizontal direction, refined to 5 km in the southern half of the Dora Maira Massif where many epicenters concentrate. The node layers in the vertical direction are at −5, 0, 5, 10, 15, 20, 30 km depth. TOMORAY requires a regular grid and we set the spacing to 10 km in the horizontal direction, and 5 km in the vertical direction.

After 6 iterations, SIMULPS leads to a variance reduction of 49% and TOMORAY to 52%. As displayed in Fig. 2, the global Rms (root mean square) of arrival

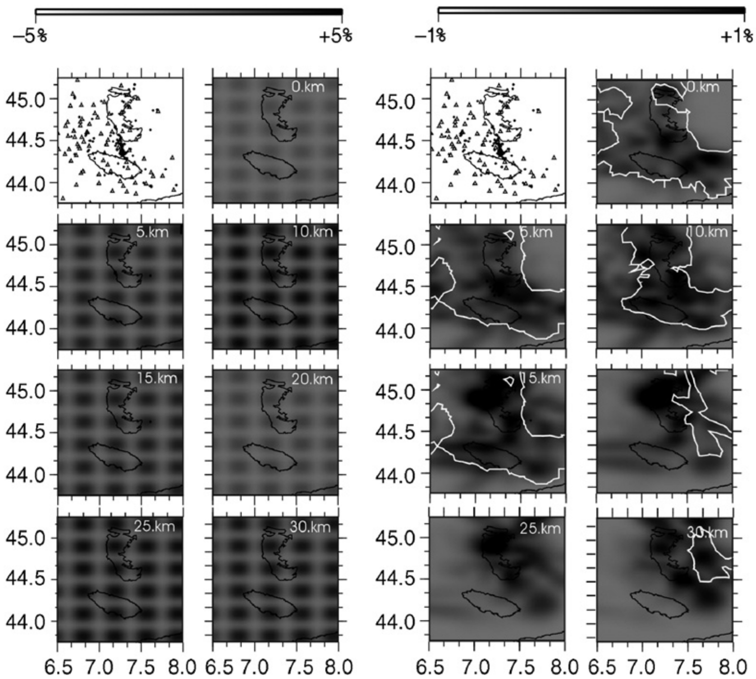

Fig. 3. Left: Depth slices of the input synthetic P-wave velocity model set up to test the resolution of the inversion with TOMORAY. Right: Depth slices of the computed 3-D P-wave velocity model using both paraxial ray tracing and LSQR. A contour of the spread function of the SIMULPS result delineating the well-resolved regions (see Paul et al., 2001) is superimposed as a white line.

times decreases strongly for the first 3 iterations. Note that the LSQR approach solves iteratively the linear system and we tested that choosing an upper limit of 500 or 5000 for the number of internal iterations does not alter the results.

Estimates of the quality of results and resolution have been largely given in Paul et al. (2001). It is not yet possible to test the results of TOMORAY with identical methods. Since LSQR is a conjugate gradient method where the generalized inverse is not solved explicitly, neither the covariance nor the resolution matrix are provided by LSQR. This limits the ability to estimate uncertainties and errors.

Nevertheless, we carried out a checkerboard sensitivity test to check the spatial resolution which is mainly related to ray density. Sinusoidal perturbations of the velocity with a wavelength of 20 km (larger than the distance between nodes) and 5% amplitude were added to the initial homogeneous medium. Fig. 3 shows the results of the inversion of synthetic travel times computed in this model. The cubic spline interpolation induces smearing of anomalies at depth were we expect smaller velocity perturbations. In the central part of the investigated area the checkerboard pattern is roughly retrieved thanks to a good ray path coverage, although anomalies have smoother shapes. In the north-eastern and south-western parts, the influence of a scarcer ray coverage is obvious. The reliability of the image decreases with depth from 5 km to 30 km with a minimum at 20 km.

Note that the areas of fair anomaly retrieval correspond to the well-resolved regions evidenced by SIMULPS. This is clear in Fig. 3 where the contours of

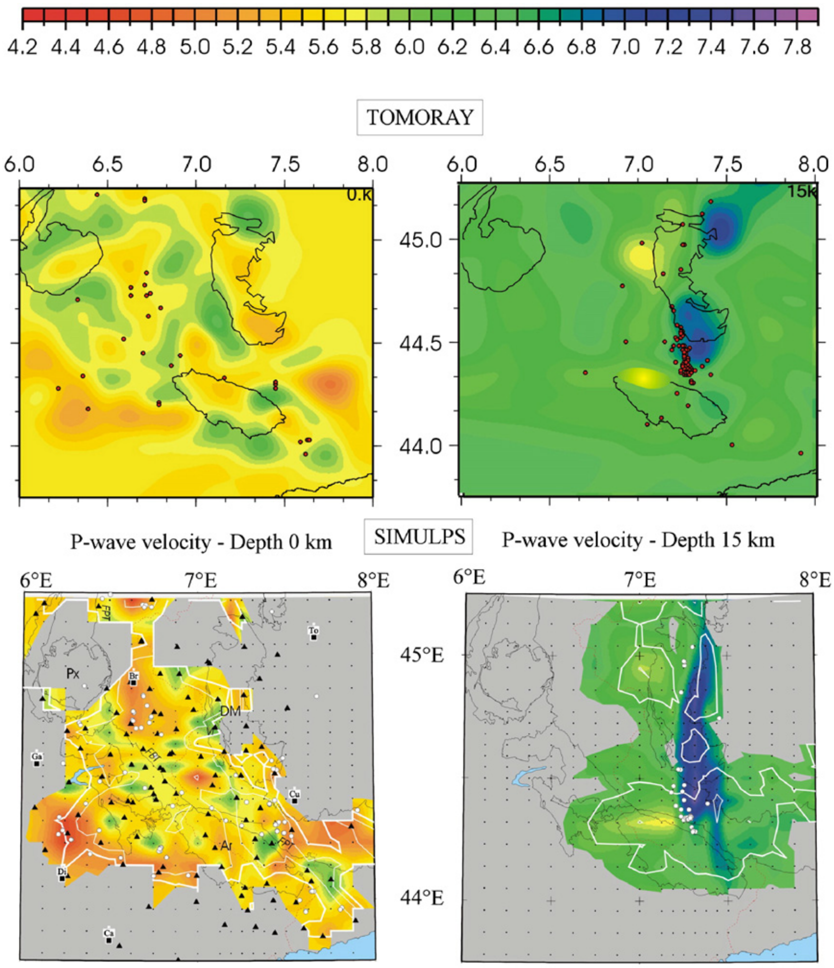

Fig. 4. Comparison of the results of the two LETs at 0 and 15 km depths. Hypocenters located in a 5-km-thick depth slice centered on the layer depth are plotted as red or white dots. The seismological stations are plotted as black triangles in the lower left hand side map. The contours of the spread function of the resolution matrix are shown as a white line and the non-resolved region are filled in grey in the SIMULPS results (see Paul et al., 2001).

the spread function of the resolution matrix chosen by Paul et al. (2001) to delineate poorly resolved areas are superimposed on the results of the checkerboard test.

2.2. Resulting velocity structures

Fig. 4 shows two map-view slices at 0 and 15 km in the 3-D velocity models computed with the two methods. As a whole, we find the same low and high velocity areas. Fig. 5 shows two cross-sections along latitude 44.1°N and longitude 7.27°E which emphasize the main feature of the crustal structure: the Ivrea body is detected as a high velocity anomaly at depths larger than 10 km in both LETs.

The image obtained by TOMORAY is smoother, due to the parameterization of the velocity model and also because the grid used with SIMULPS is finer (5 km) in the center of the area. Consequently, the velocity contrasts are weaker with TOMORAY because of the different gridding and the b-spline interpolation. The discrepancies in velocity reach 0.3 km/s in the Ivrea body but are generally of the order of 0.1 km/s. The difference in grid spacing does not explain why TOMORAY is unable to image the deepest part of the Ivrea body (under 25 km) whereas the checkerboard test showed that the resolution was fair at these depths. We think that this failure is due to the sharp velocity contrast in the Ivrea body, which induces a lack of computed ray-paths in this

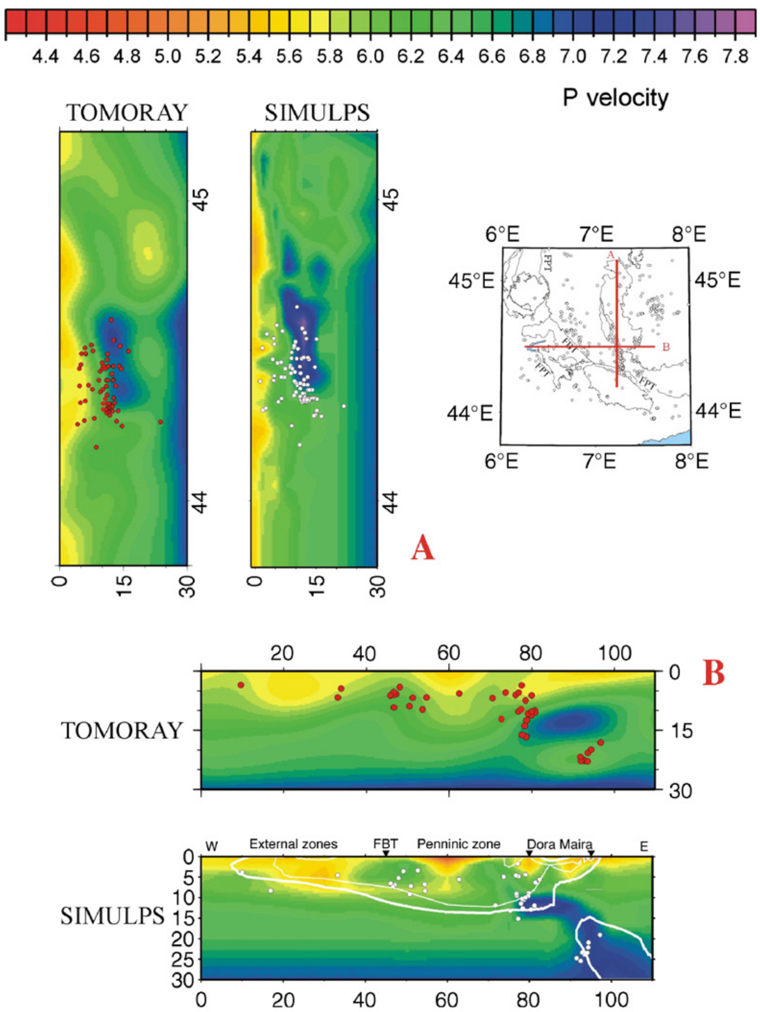

Fig. 5. Comparison of the two 3-D velocity models along two cross-sections cross-cutting the Ivrea body. The locations of these sections are shown on the map. The red (on TOMORAY result) and white (on SIMULPS result) dots correspond to hypocenters located in a 10-km wide section, orthogonally projected onto the transects. The contours of the spread function delineated by a white line are reported on the E–W section corresponding to the SIMULPS result.

Table 1
Locations and focal solutions computed in the minimum 1-D model

	Date	H mn	Sec latitude	Longitude	Depth	Rms	Az1	Dip1	Rake1	Az2	Dip2	Rake2	Azp	Dipp	Azt	Dipt
B1	960801	0013	3.37 45n16.0	6e17.9	2.44	0.56	170	65	−150	66	63	−28	299	38	208	1
P1	960809	1714	38.21 44n27.8	7e16.1	9.83	0.23	155	70	−10	249	80.6	−160	23	21	290	7
E1	960809	1731	16.22 44n23.2	6e25.0	5.92	0.3	80	80	−170	348	80	−10	214	14	304	0
E2	960809	1840	53.86 44n22.9	6e24.1	8.69	0.2	75	50	−130	308	54	−53	188	60	282	2
P2	960811	0825	12.23 44n33.7	7e11.4	6.91	0.21	55	70	−150	314	62	−23	187	35	93	5
A1	960812	0913	12.37 44n17.6	7e29.0	3.92	0.13	142	44	83	332	46	97	313	85	51	1
P3	960817	1929	7.00 44n21.1	7e17.8	13.45	0.23	160	90	60	70	30	180	187	38	313	38
P4	960817	2005	19.04 44n22.1	7e16.0	13.14	0.2	245	50	−100	80	41	−78	12	81	252	5
B3	960822	1614	50.35 44n28.0	6e54.8	4.7	0.25	120	70	20	23	71	159	342	1	251	28
P5	960823	0554	38.65 44n27.3	7e16.6	11.11	0.24	100	75	−140	358	52	−19	236	38	134	15
P6	960902	0008	37.37 44n22.8	7e15.2	14.85	0.28	215	45	−140	94	63	−53	323	55	68	10
P7	960902	1700	34.28 44n22.5	7e14.7	14.27	0.21	275	30	−80	84	61	−96	249	74	88	15
B4	960903	1400	38.92 44n32.0	6e40.2	5.4	0.16	205	40	−90	25	50	−90	205	85	25	5
B5	960908	1746	23.5 44n23.2	6e51.7	7.77	0.25	240	30	−110	83	62	−79	287	71	75	16
B6	960909	0813	24.39 44n29.9	6e53.1	10.15	0.13	65	75	−150	327	61	−17	199	32	103	9
P8	960911	0540	38.74 44n20.9	7e17.8	12.62	0.21	130	70	−40	236	52.8	−155	357	42	97	11
B7	960912	0846	23.72 44n33.1	6e49.5	8.75	0.26	75	65	−130	318	46	−36	207	52	103	11
P9	960920	2205	23.42 44n32.5	7e15.5	12.18	0.19	75	60	−160	335	73	−32	201	34	297	8
B2	960926	1105	40.51 44n52.6	6e22.0	8.01	0.36	95	65	−160	356	72	−26	224	31	317	5
P10	960928	1548	8.46 44n33.7	7e 8.2	9.17	0.31	250	85	120	349	30	10	225	33	99	42
E3	961007	0213	25.02 44n13.1	6e48.5	7.93	0.34	265	50	−110	115	44	−68	20	74	279	3
P11	961022	0339	53.48 44n58.5	7e 1.8	9	0.32	110	60	−110	326	36	−59	249	68	124	13
B8	961025	0613	11.27 44n30.7	6e50.5	8.13	0.19	245	35	−60	30	60.2	−109	170	69	44	13
E4	961026	1621	58.41 44n12.4	6e48.0	3.4	0.32	115	70	−60	236	35.5	−144	333	55	93	19
P12	961027	1011	4.38 44n20.6	7e17.0	13.09	0.23	100	50	−110	310	44	−68	215	74	114	3
B9	961028	0735	31.48 45n16.2	6e32.4	7.97	0.26	160	65	−90	340	25	−90	340	70	160	20
P13	961103	1904	12.66 44n39.9	7e11.5	10.82	0.34	80	70	−120	319	36	−36	222	55	102	19
P14	961103	2001	24.52 44n23.7	7e12.5	11.29	0.27	235	60	−70	19	35.5	−121	96	68	221	13
B10	961105	0332	20.77 45n15.8	6e31.5	7.99	0.35	95	30	−80	264	61	−96	69	74	268	15
A2	961105	2038	19.12 44n45.5	7e22.3	19.51	0.10	57	82	−116	312	27	−17	299	46	169	32
P15	961115	2317	40.54 44n17.9	7e18.4	15.47	0.34	260	25	−60	48	68.5	−103	206	64	58	22
P16	961115	2335	14.97 44n17.9	7e18.2	15	0.3	215	50	−130	88	54	−53	328	60	62	2
A3	961122	2224	49.76 44n45.1	7e28.9	25.31	0.05	9	77	−157	274	68	−14	233	24	140	
P17	961123	1049	27.19 44n39.8	7e11.5	9.38	0.29	260	30	−70	57	62	−101	213	71	65	16
P18	961125	0839	31.03 44n30.6	7e14.7	11.99	0.18	130	40	170	228	84	50	258	28	13	38
E5	961201	1123	29.21 44n12.4	6e47.5	4.73	0.19	105	75	−20	200	70.7	−164	332	25	63	3
P19	961211	1750	41.84 44n50.9	7e15.7	16.47	0.35	175	45	−60	316	52.2	−117	74	69	334	4
P20	961212	1625	58.11 44n26.6	7e14.7	12.5	0.17	120	65	−120	354	38	−43	257	59	141	15
B11	961215	0356	10.93 44n32.3	6e50.1	8.05	0.21	350	80	0	260	90	170	215	7	125	7
P21	961216	0522	37.86 45n 2.8	7e18.1	16.17	0.32	130	50	−140	12	61	−48	245	53	343	6
A4	961226	1933	49.67 44n21.1	7e18.2	14.86	0.3	65	70	−160	328	71	−21	196	28	287	1
P22	961226	1938	40.61 44n20.4	7e17.4	14	0.18	80	75	160	175	71	16	38	3	307	25
P23	961226	1958	51.23 44n20.1	7e16.9	13.49	0.16	0	90	40	270	50	180	37	27	143	27
E6	961229	1018	40.72 44n01.3	7e36.2	5.00	0.94	123	85	87	330	6	117	215	40	30	50
B12	961230	1122	38.42 44n37.8	6e42.1	5.36	0.28	170	55	−20	272	73.7	143	46	37	307	12

part of the medium. As previously shown by Haslinger and Kissling (2001), the paraxial ray tracing may fail if either source or receiver is located close to a strong velocity contrast. We observe the same behaviour for a few rays coming from the deepest events located close to the Ivrea body. Since the shooting of a significant number of rays fails in the deepest part of the model, velocity parameters are not inverted by TOMORAY.

2.3. Comparison of hypocenter locations

We now compare the discrepancies in earthquake locations in the most active areas: the Briançonnais units, the Piemont area and the western part of the study region. In the two last regions, locations of hypocenters should be strongly affected by the 3-D velocity model since corresponding rays propagate across the strong velocity

Table 2
Locations and focal solutions computed in the SIMULPS 3-D model

	Date	H mn	Sec	latitude	Longitude	Depth	Rms	Az1	Dip1	Rake1	Az2	Dip2	Rake2	Azp	Dipp	Azt	Dipt
B1	960801	0013	3.58	45n16.79	16.85	−0.49	0.06	150	80	−57	255	34	−162	93	45	214	28
P1	960809	1714	38.37	44n27.62	7e16.22	6.99	0.09	159	73	−174	67	84	−17	202	17	114	9
E1	960809	1731	16.35	44n23.10	6e24.30	5.92	0.12	240	45	−54	15	55	−120	228	65	126	6
E2	960809	1840	53.64	44n22.77	6e23.52	5.67	0.1	227	63	−40	338	55	−146	189	47	284	5
P2	960811	0825	12.34	44n33.85	7e10.56	5.38	0.06	18	58	−48	138	51	−137	344	55	79	4
A1	960812	0913	12.65	44n17.70	7e29.07	4.88	0.26	142	44	83	332	46	97	57	1	313	85
P3	960817	1929	7.1	44n20.78	7e17.21	13.25	0.09	238	84	−43	334	47	−172	185	35	295	25
P4	960817	2005	19.26	44n21.64	7e15.34	12.3	0.07	248	43	−102	344	48	−79	319	82	66	3
B3	960822	1614	50.29	44n27.92	6e54.48	3.39	0.06	293	74	162	28	73	17	341	1	250	24
P5	960823	0554	39.87	44n27.00	7e16.69	8.65	0.07	264	55	−20	6	74	−143	231	38	131	13
P6	960902	0008	37.49	44n22.30	7e14.08	13.94	0.09	121	35	−137	354	67	−63	303	59	64	18
P7	960902	0017	34.39	44n22.24	7e14.12	13.79	0.07	154	22	−120	6	71	−79	294	62	87	25
B4	960903	0140	38.89	44n31.86	6e39.80	4.21	0.1	290	43	−81	98	48	−98	308	83	194	3
B5	960908	1746	29.61	44n23.14	6e51.08	6.51	0.09	184	30	−78	350	61	−97	243	73	85	15
B6	960909	0813	24.36	44n29.73	6e52.98	9.17	0.07	65	75	−150	327	61	−17	199	32	103	9
P8	960911	0540	38.87	44n20.73	7e17.30	13.36	0.07	333	58	−145	223	61	−37	187	46	279	2
B7	960912	0846	23.78	44n33.10	6e49.13	7.37	0.08	247	63	−42	359	53	−146	209	48	305	6
P9	960920	2205	23.64	44n32.27	7e13.89	12.83	0.07	242	76	−37	342	54	−163	196	35	296	15
E2	960926	1105	40.46	44n52.05	6e21.18	3.25	0.08	261	34	−18	6	80	−123	243	45	122	27
P10	960928	1548	8.5	44n33.82	7e07.62	7.48	0.12	157	80	95	310	11	63	243	35	73	55
E3	961007	0213	24.95	44n12.88	6e47.33	−2.3	0.15	207	46	−59	346	52	−118	193	68	96	3
P11	961022	0339	53.41	44n58.37	7e01.22	8.07	0.09	230	40	−77	33	51	−101	253	80	131	5
B8	961025	0613	11.18	44n30.38	6e50.28	6.49	0.11	295	67	−106	151	28	−57	178	64	37	20
E4	961026	1621	58.34	44n12.14	6e47.24	−1.92	0.1	165	49	−97	356	41	−82	28	83	264	4
P12	961027	1011	4.51	44n20.51	7e16.16	12.02	0.07	144	88	147	234	84	2	189	4	99	4
B9	961028	0735	31.61	45n16.44	6e32.52	2.74	0.07	78	79	−83	225	13	−122	357	55	162	34
P13	961103	1904	12.84	44n39.91	7e10.76	7.8	0.08	339	89	−110	246	20	−3	231	43	86	41
P14	961103	2001	24.62	44n23.31	7e12.45	13.08	0.07	298	38	−143	177	68	−58	128	55	244	17
B10	961105	0332	20.86	45n15.97	6e30.97	6.31	0.08	169	53	−99	4	38	−78	41	79	268	8
A2	961105	2038	19.27	44n45.59	7e22.37	19.51	0.1	223	74	109	352	25	42	298	26	158	57
P15	961115	2317	15.2	44n17.32	7e18.08	15.2	0.07	210	26	−23	321	80	−114	205	49	71	31
P16	961115	2335	15.13	44n17.22	7e18.20	15.39	0.07	165	33	−83	337	57	−95	233	78	70	12
A3	961122	2224	49.79	44n45.17	7e28.99	25.31	0.05	134	58	72	346	36	117	237	12	3	71
P17	961123	1049	27.26	44n39.80	7e10.94	7.67	0.08	139	13	−119	349	79	−84	267	56	74	34
P18	961125	0839	21.64	44n30.91	7e14.90	9.74	0.04	350	7	97	163	83	89	254	38	72	52
E5	961201	1123	29.28	44n12.4	6e47.5	4.73	0.19	106	76	−117	351	30	−29	345	51	217	26
P19	961211	1750	41.94	44n51.21	7e14.46	14.55	0.07	228	39	−117	81	56	−70	39	71	157	9
P20	961212	1625	53.31	44n26.68	7e14.47	10.97	0.07	255	33	−39	19	70	−117	254	57	129	21
B11	961215	0356	10.97	44n32.29	6e49.87	6.8	0.1	173	76	−144	73	55	−17	39	35	299	14
P21	961216	0522	37.9	45n01.77	7e18.23	15.08	0.08	294	79	−37	32	54	−166	247	33	348	16
A4	961226	1933	49.76	44n20.69	7e17.55	14.93	0.08	244	47	10	148	83	137	203	22	98	33
P22	961226	1938	40.79	44n20.47	7e17.17	13.96	0.08	284	40	61	140	56	112	214	8	100	70
P23	961226	1958	51.45	44n20.51	7e17.12	14.06	0.09	147	56	144	259	61	40	22	3	115	48
E6	961229	1018	40.61	43n59.71	7e34.81	−1.73	0.07	148	59	111	291	37	59	223	12	102	68
B15	961230	1122	38.42	44n37.78	6e41.64	3.59	0.09	196	40	−137	70	64	−59	25	59	138	14

anomaly of the Ivrea body. Concerning epicenter positions, we obtain very similar results using the minimum 1-D model and the results of the two 3-D inversions. Tables 1 (1-D locations), 2 (SIMULPS locations), and 3 (TOMORAY locations) display the focal parameters of 46 events. The lateral shifts are of few hundreds of meters. The differences in depth are more important. The differences between the 1-D, TOMORAY and SIMULPS 3-D models are presented as histograms in Fig. 6. Comparing 1-D and SIMULPS locations (Fig. 6-A), we find a depth shift smaller than 2 km for a majority of events. Hypocenters located in the 3-D model are shallower. This shift is rather small in the Briançonnais zone which is not affected by strong velocity anomalies, but it reaches 4 km (for the deepest events) in the Piemont or the external zones, where strong velocity contrasts are observed. The comparison between 1-D and TOMORAY locations (Fig. 6-B), shows that the depth shifts are more

Table 3
Locations and focal solutions computed in the TOMORAY 3-D model

	Date	H mn	Sec	latitude	Longitude	Prof	Rms	Az1	Dip1	Rake1	Az2	Dip2	Rake2	Azp	Dipp	Azt	Dipt
B1	960801	0013	3.61	45n17.65	6e16.00	0.43	0.21	149	80	−57	254	34	−162	92	45	213	27
E1	960809	1731	16.4	44n22.9	6e24.0	5.63	0.18	240	45	−54	15	55	−120	228	65	126	50
E2	960809	1840	53.96	44n23.14	6e24.86	3.86	0.18	19	68	−98	220	23	−71	275	66	275	60
P2	960811	0825	12.25	44n33.85	7e11.4	5.05	0.21	26	59	−49	147	50	−137	350	56	88	6
A1	960812	0913	12.54	44n18.06	7e29.16	4.8	0.26	143	46	103	305	46	77	44	0	132	81
P3	960817	1929	7.77	44n21.11	7e17.89	11.34	0.32	235	83	−43	331	47	−170	185	33	290	22
P4	960817	2005	18.11	44n22.24	7e16.32	12.61	0.28	172	44	−81	340	47	−99	178	84	76	1
B3	960822	1614	50.36	44n28.36	6e54.66	4.11	0.24	33	70	29	292	63	157	161	5	251	39
P5	960823	0554	39.77	44n27.3	7e16.6	11.11	0.24	5	65	−143	257	57	−30	224	44	129	5
P6	960902	0008	37.49	44n23.32	7e15.66	11.55	0.21	1	73	−81	153	19	−117	284	61	84	27
P7	960902	1700	34.36	44n22.5	7e14.7	12.8	0.21	11	63	−63	143	37	−132	324	62	82	14
B5	960908	1746	29.55	44n22.54	6e51.75	7.17	0.13	117	26	−118	328	67	−77	260	65	48	21
B6	960909	0813	24.42	44n29.87	6e53.27	9.24	0.1	225	47	−43	347	60	−128	205	56	103	8
P8	960911	0540	38.88	44n21.03	7e17.99	11.64	0.19	327	58	−143	215	59	−38	181	48	271	1
B7	960912	0846	23.81	44n33.39	6e50.24	10.14	0.03	234	51	−37	349	62	−135	207	51	109	7
P9	960920	2205	23.49	44n32.19	7e14.74	11.57	0.11	238	53	−35	351	63	−137	209	49	112	6
B2	960926	1105	40.69	44n52.26	6e22.31	7.47	0.25	263	77	−43	5	48	−163	215	39	320	18
P10	960928	1548	08.50	44n33.58	7e07.96	6.36	0.11	159	85	98	281	9	32	242	39	78	39
E3	961017	1521	39.11	43n59.48	7e31.72	10.99	0.16	134	88	130	46	40	3	12	31	257	34
P11	961022	0339	53.44	44n58.18	7e01.19	8.44	0.14	28	50	−103	228	42	−75	240	79	127	4
B8	961025	0613	11.3	44n30.7	6e50.5	5.98	0.19	156	33	−57	298	63	−109	172	66	42	16
E4	961026	1621	05.80	44n12.14	6e47.34	1.92	0.1	165	49	−97	356	41	−82	28	83	264	4
P12	961027	1011	4.5	44n20.65	7e16.14	12.16	0.08	327	73	−143	225	55	−21	192	37	92	12
B9	961028	0735	31.57	45n16.31	6e32.15	4.51	0.12	81	80	−83	226	12	−125	359	54	165	35
P13	961103	1904	12.64	44n39.85	7e11.52	8.95	0.17	33	86	79	283	12	160	133	40	291	48
P14	961103	2001	24.71	44n23.26	7e12.81	12.09	0.11	175	70	−60	296	36	−144	123	55	243	20
B10	961105	0332	20.87	45n16.13	6e30.80	5.87	0.12	5	37	−83	176	53	−96	62	81	270	8
A2	961105	2038	19.05	44n45.58	7e21.96	20.5	0.14	237	88	124	329	34	3	292	28	183	32
P15	961115	2317	40.57	44n17.44	7e18.78	15.94	0.9	180	25	−61	328	68	−103	217	64	68	22
P16	961115	2335	15.04	44n17.49	7e18.66	15.45	0.1	334	66	−103	184	27	−63	220	66	74	20
A3	961122	2224	49.74	44n44.83	7e28.84	23.43	0.14	6	65	−157	266	69	−27	225	33	317	3
P17	961123	1049	27.23	44n39.56	7e11.41	7.59	0.14	148	5	−103	341	85	−89	251	45	71	45
P18	961125	0839	21.44	44n31.06	7e14.83	10.71	0.11	46	22	−177	313	89	−68	244	42	23	40
P19	961211	1750	42.04	44n50.68	7e14.57	13.19	0.17	76	50	−77	236	42	−105	44	79	157	4
P20	961212	1625	58.19	44n26.86	7e14.99	11.33	0.11	261	31	−32	19	74	−117	256	53	130	24
B11	961215	0356	11.09	44n32.43	6e49.83	6.05	0.15	353	70	−137	245	50	−26	217	44	115	12
P21	961216	0522	37.6	45n02.02	7e18.27	16.14	0.16	288	82	−42	25	49	−169	238	34	343	21
A4	961226	1933	49.67	44n21.28	7e18.90	14.1	0.22	65	70	−160	328	71	−21	196	28	287	1
P22	961226	1938	40.64	44n20.29	7e18.16	14.55	0.23	80	75	160	175	71	16	38	3	307	25
P23	961226	1958	51.24	44n20.91	7e17.85	14.6	0.27	0	90	40	270	50	180	37	27	143	27
E6	961129	1018	41.14	44n02.04	7e34.77	−1.03	0.31	166	36	100	334	55	83	69	9	217	79
B12	961230	1122	38.52	44n37.72	6e42.02	3.36	0.12	189	63	−117	57	37	−48	56	62	298	14

concentrated between 1 and 2 km. Comparing SIMULPS and TOMORAY locations (Fig. 6-C), we see that most differences in depth are concentrated between 0 and 1 km. There is no systematic trend with events being shifted toward the surface or to greater depths. As shown in Tables 2 and 3 and, the corresponding depths are often very close to each other for the strongest magnitude events located with enough data to compute focal mechanisms.

The question is now to determine whether the shifts in hypocenter depths observed with the TOMORAY and SIMULPS codes (Fig. 6-C) are due to differences in methodology. We compared the locations computed by SIMULPS with those computed by the same program using the so-called "gradational approach". As explained by Paul et al. (2001), it consists in successive series of inversions on more and more detailed grids. The histograms of depth shifts of Fig. 6-D show here again that most differences are smaller than 1 km and often around 500 m. We therefore think that differences in locations result more from discrepancies in the velocity model than from the methodologies used.

Fig. 7 shows hypocenters computed in the 3 velocity models and projected onto an E–W cross-section. It confirms that although no dramatic change in the

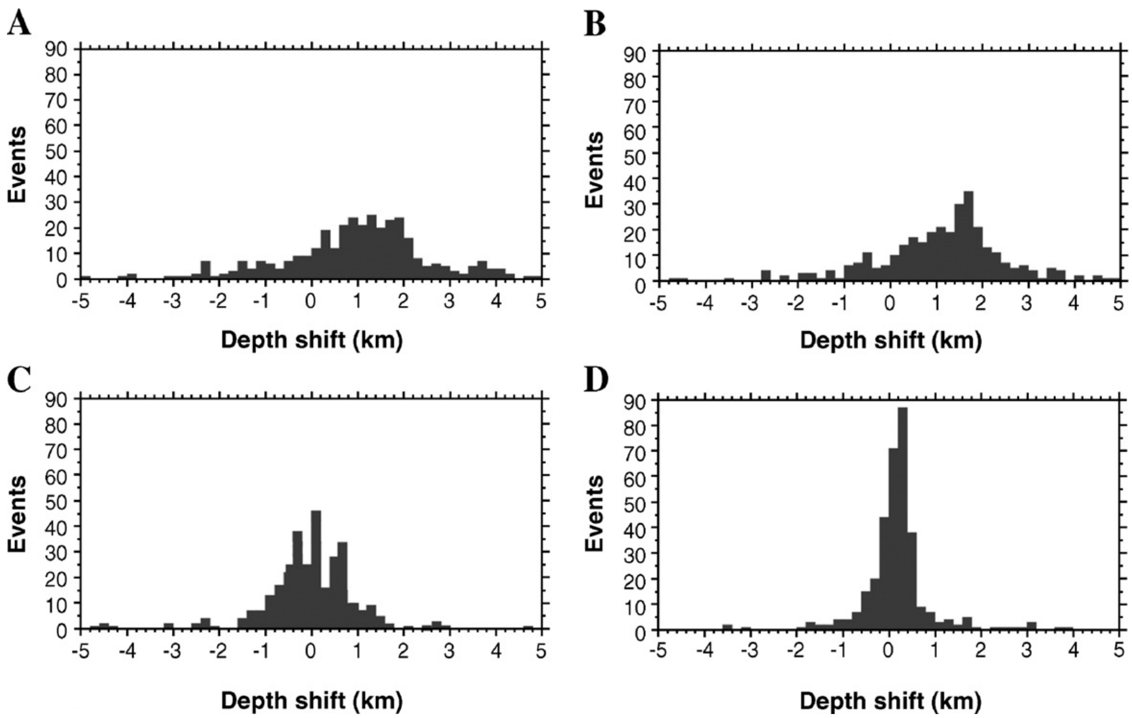

Fig. 6. Histograms of depth shifts between the different hypocentral locations. A: depth shifts between 1-D and SIMULPS locations; B: depth shifts between 1-D and TOMORAY locations; C: depth shifts between SIMULPS and TOMORAY locations; D: depth shifts between SIMULPS direct inversion and SIMULPS gradational inversion.

general distribution of events results from the change in velocity model, small shifts in depth can be detected mainly for the deepest events of the Piemont zone.

2.3.1. *Focal mechanisms*

The map of Fig. 1 shows that the main characteristics of the instrumental seismicity map of the western Alps are retrieved in the distribution of epicenters recorded during the GéoFrance 3-D experiment. The two seismic arcs discovered and named Briançonnais and Piemont arcs by Rothé (1941), are clearly drawn. We will thus use letter B for events of the Briançonnais units and P for the Piemont units. The few events with a more diffuse distribution in the Southern External Alps will be referenced with letter E. Earthquakes located in the eastern part of the study area, mainly under the Po basin, will be referenced using letter A (see Fig. 8 for a delineation of these different regions). The 46 computed focal solutions depend on the depth and take-off angles which should vary from one model to another (Tables 1, 2, and 3).

2.3.1.1. The Briançonnais units. Focal solutions in this region are normal or strike slip mechanisms (Figs. 8 and 9). About half of the solutions obtained with the 1-D,

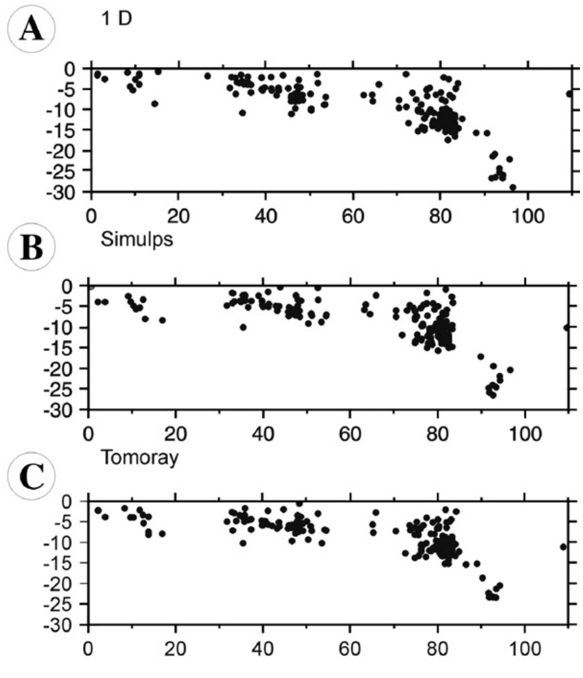

Fig. 7. Projection of all hypocenters on an E–W vertical cross-section. A: 1-D model locations, B: SIMULPS locations, C: TOMORAY locations.

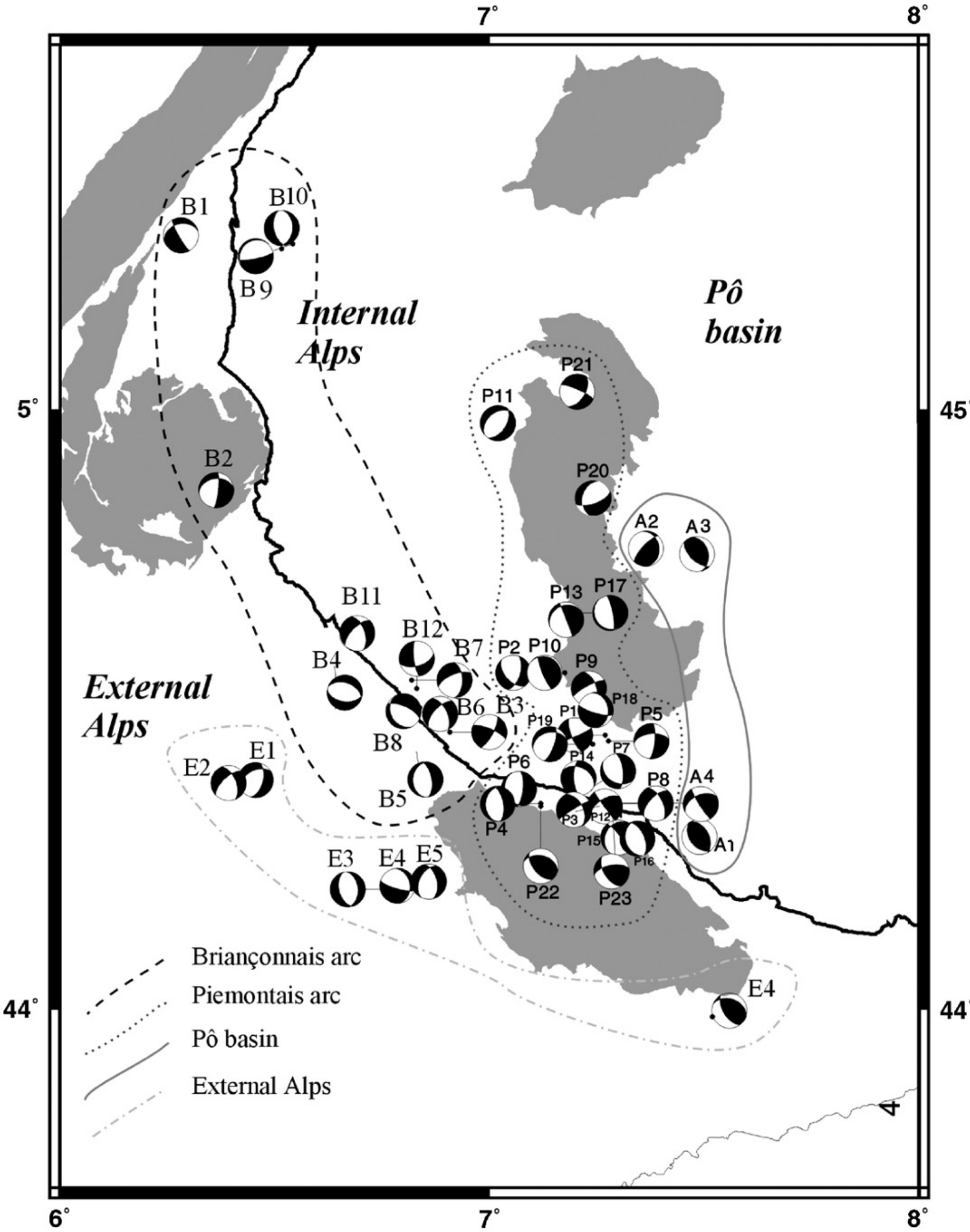

Fig. 8. Locations of the focal solutions computed with TOMORAY. Earthquakes are divided in 4 groups A, B, E, and P, where A stands for «Po basin», B for «Briançonnais units», E for «External area», and P for «Piemont units». Solutions B1, P1, and E4 were computed with SIMULPS.

3-D SIMULPS and 3-D TOMORAY model are very close to each other (see for example B3, B5, and B10 events). Focal mechanisms B1 and B9 are rather ill-constrained and the differences observed in the solutions are within the error limits. TOMORAY does not provide enough rays to compute a well-constrained solution for B4. Other solutions are well-constrained. Error computations with the FPFIT code give strike uncertainties from 5° to 10°, and dip uncertainties from 5° to 15°. The differences in solutions for B2, B6, and B11 obtained with the 1-D and 3-D models are due to changes in the incidence angle of the rays and not to uncertainties on the strike and dip of the nodal planes. The two sets of 3-D solutions (Fig. 9-B and C) are very close to each other,

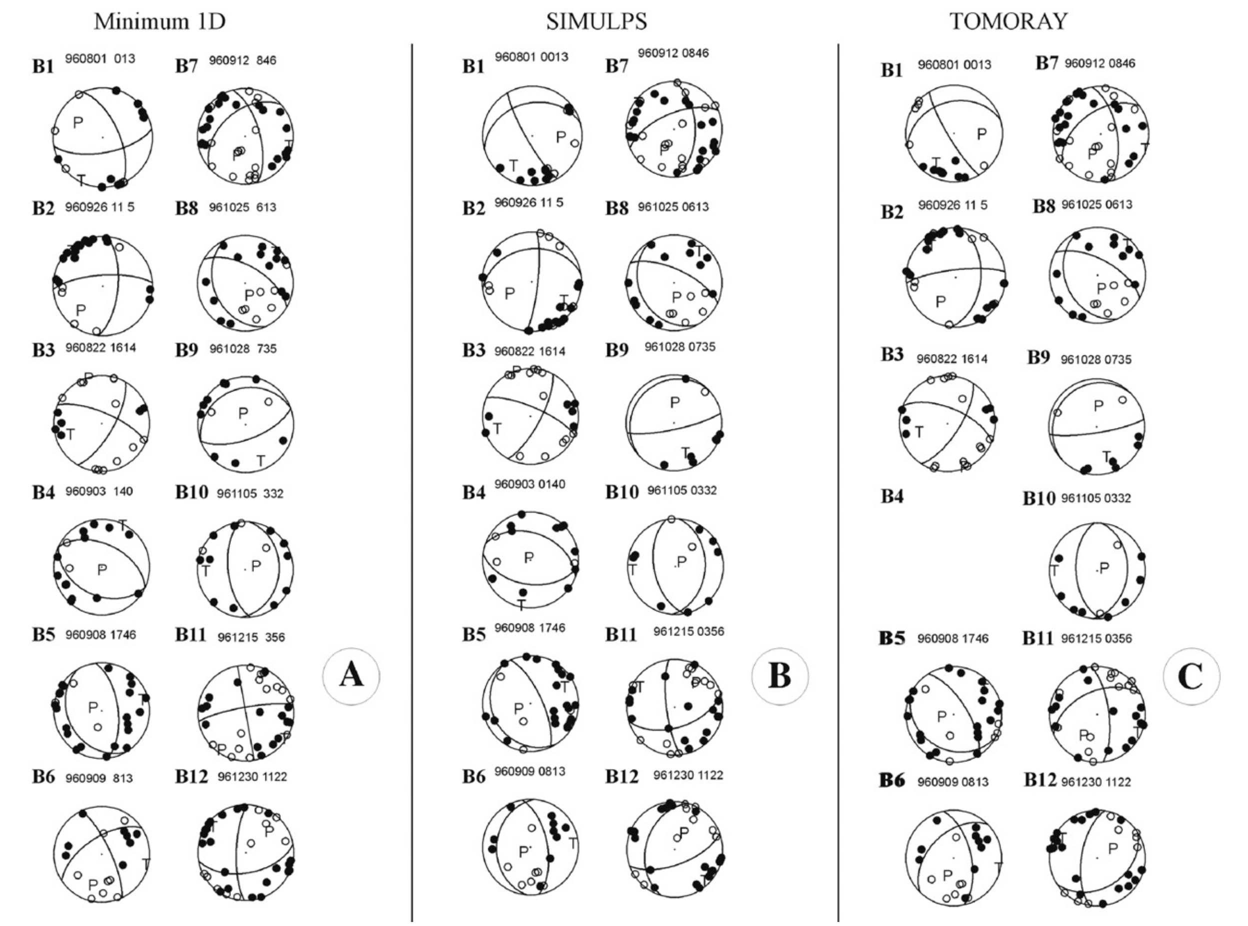

Fig. 9. Comparison of focal solutions for the "Briançonnais" events, as obtained in the 1-D, SIMULPS and TOMORAY velocity models.

with a normal component increased with respect to the 1-D solution, introducing more strike slip in the mechanisms. We observe that solution C (obtained with the paraxial ray tracing) computed for B11 event is better constrained, due to rather important changes in the computed incidence angles. It is more coherent with the solutions of neighbour events than the solution computed with the pseudo-bending ray tracing. Anyway, both 3-D focal mechanisms lead to a normal faulting solution with the same P and T axes.

In summary, the take-off angles are slightly shifted but no dramatic change is observed in the position of the nodal planes. However a better coherency of the different focal solutions is obtained even if, in this case, the 3-D computations do not improve significantly the knowledge of the local stress field.

2.3.1.2. The Piemont units. In this area, the shifts in depth between the 3 sets of locations reach 2 or 3 km due to their location close to the strong velocity anomaly of the Ivrea body. This anomaly also has a key influence on the determination of the focal solutions. The TOMORAY inversion generally gives focal depths 1 km shallower than the SIMULPS inversion, which in turn gives focal depths shallower than the 1-D model solutions. Some rays from the deepest earthquakes propagate through a very heterogeneous medium, implying significant changes of take-off angles computed in the 3-D model. The P1 mechanism which was computed from a small number of picks could not be computed with TOMORAY because of the lack of rays due to instabilities of the paraxial ray tracing.

Consequently, we expect more important changes between the 3 series of focal mechanisms than in the Briançonnais area. We observe larger differences between the 1-D and the 3-D solutions: strike and dip of the focal planes differ generally by about 20°. However, for P8 event the nodal planes computed in 1-D model and 3-D models have different orientations. 3-D solutions P7 and P8 are better constrained than the corresponding 1-D mechanisms.

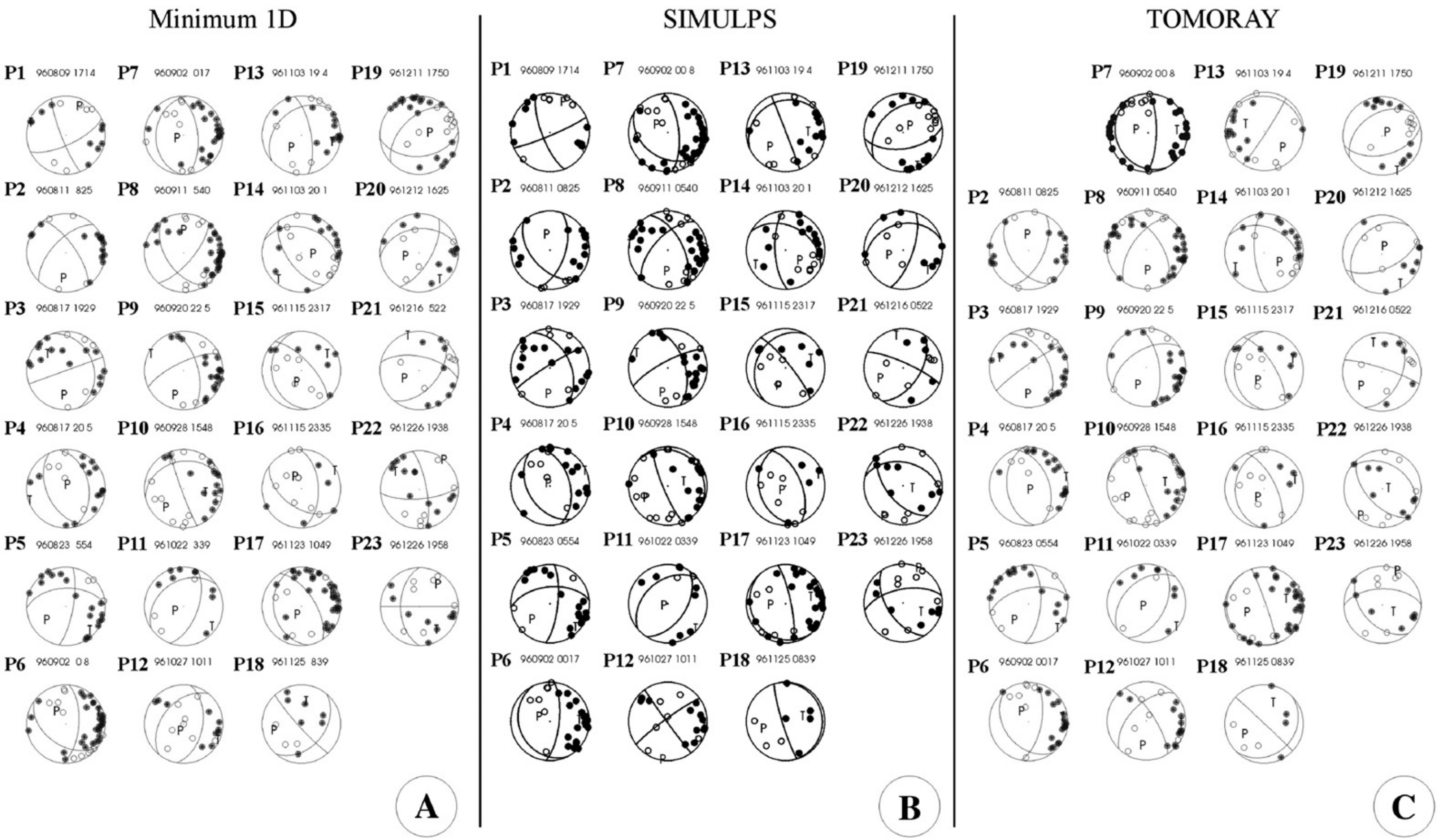

Fig. 10. Same legend as Fig. 9 for the "Piemont" events.

On the other hand, a remarkable similarity is observed between the two 3-D solutions (Fig. 10). Despite the changes in focal depth and slight change in take-off angles, the distribution of polarities remains coherent and the nodal planes computed by the FPFIT code (Reasenberg and Oppenheimer, 1985) correspond to very similar focal mechanisms. However, solutions obtained with TOMORAY for P12 and P18 events are slightly better constrained and seem more realistic from a geological point of view than those obtained with the SIMULPS code.

Nevertheless, if the details of the focal solutions generally differ between the 1-D and 3-D models, the tectonic conclusions (nature of the faults, directions of *P* and *T* axes) remain similar. A majority of mechanisms have a normal component, except P10, P22, and P23 events which have inverse solutions.

2.3.1.3. The Po basin events. It was not possible to compute focal solutions for the deepest earthquakes located below the western edge of the Po basin, due to their low magnitude and the emergent character of the P-wave arrivals. The best seismograms are shown by Cattaneo et al. (1999) who studied this deep seismicity. However they did not have enough readable polarities to compute focal solutions. Here, we could analyze a few focal mechanisms obtained for events located east of the Piemont units (events A in Figs. 8 and 11).

Except for A1 event, hypocenters are rather deep (between 10 and 26 km). Again, we only observe small discrepancies between the two 3-D solutions. The 1-D solutions are close to strike slip components, whereas the 3-D mechanisms display a compressive character.

2.3.1.4. The external zone. Six focal mechanisms correspond to events located in the external Alps (events E in Fig. 8). E1 solution turns to a normal solution in the 3-D computations and becomes very close to E2 solution (Fig. 12). TOMORAY does not provide enough rays to obtain a well-constrained solution for E5 event. The 1-D location fails in the computation of a realistic solution for E4 event, which occurred too close to the southern boundary of the seismological network. The 3-D take-off angles are more coherently distributed even if the focal solution remains ill-constrained.

3. Tectonic implications

Although data used in this study were recorded during a small-duration experiment (5 months), the main characteristics of the seismicity map are very similar to those of the seismological catalogues which document the earthquake activity for almost fifty years. This demonstrates the permanent activity of the Briançonnais and Piemont units. Moreover, local earthquake tomography leads to a refined image of this seismicity. Fig. 13 shows a depth cross-section, trending in a W–E direction along latitude 44.6°N (see location in Fig. 1). We superimpose on the velocity structure the hypocenters located less than 25 km away from the cross-section.

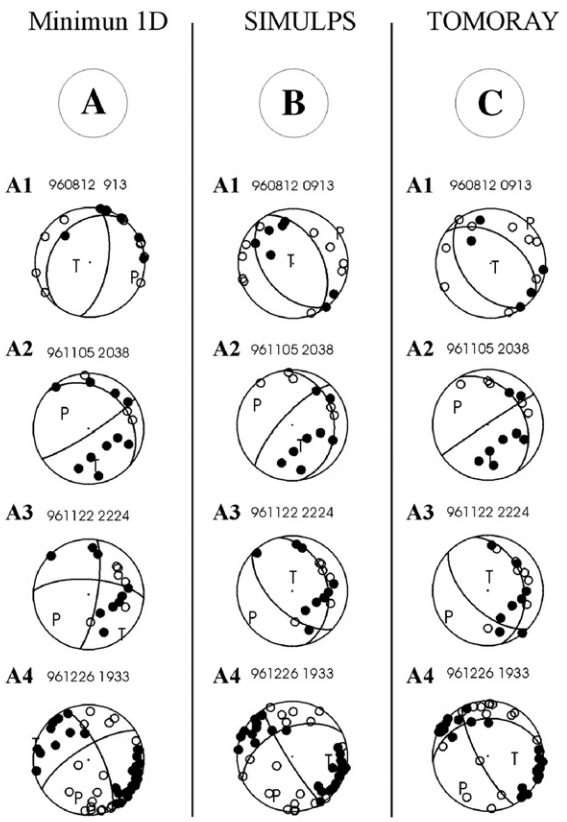

Fig. 11. Same legend as Fig. 9 for the "Po basin" events.

The computed focal depths range between 0 and 10 km west of the Pelvoux and Argentera massifs and in the Internal Zone. Beneath the Dora Maira massif, the Piemont units exhibit focal depths from 0 to 15 km (Fig. 13). Events located more to the east are deeper between 20 and 25 km (Figs. 7 and 13), within a narrow stripe orientated N–S. Deichmann et al. (2000) emphasize the singularity of such deep earthquakes in the western Alps, where no significant lower crustal seismicity is usually observed. Note that these events were already relocated by Solarino et al. (1997) and plotted on the cross-sections published by Schmid and Kissling (2000). So, the main result of our two tomography studies (Paul et al., 2001, and this paper), is the explanation of the

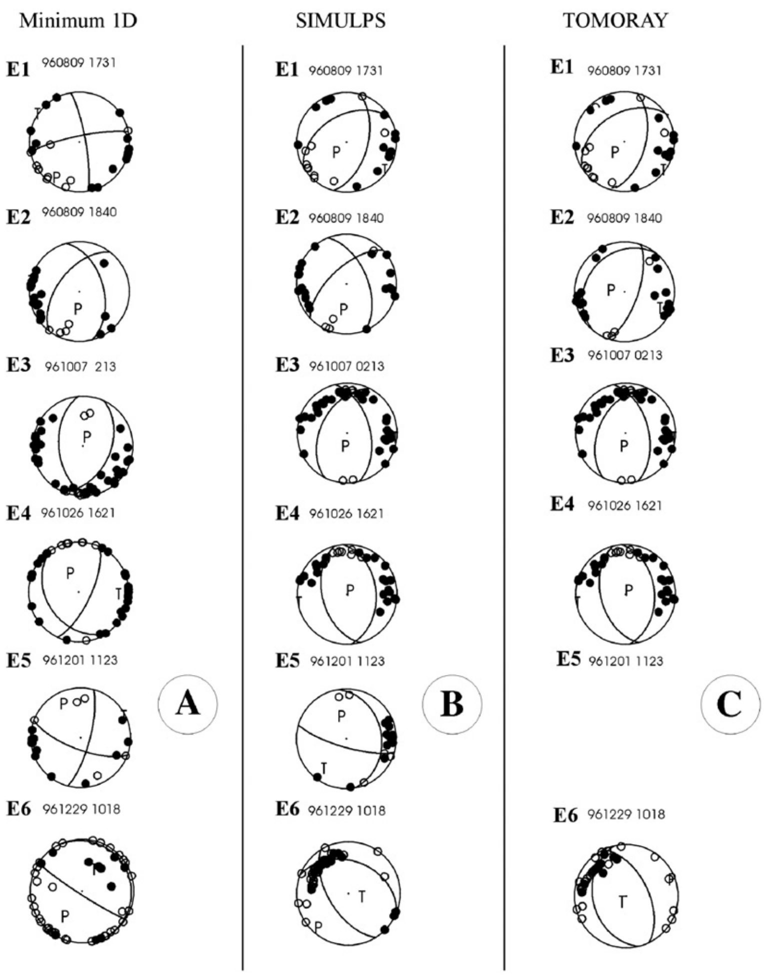

Fig. 12. Same legend as Fig. 9 for the “External” events.

seismicity of the Piemont units, trending north–south (Fig. 1), which corresponds to none of the surface geological structures (see for example the geological map of GAP, 1/25000). The SIMULPS tomography gives a detailed image of the Ivrea body which is north–south orientated in this region. We can then infer that earthquakes of the Piemont units concentrate on the western boundary of the high velocity anomaly of the Ivrea body (see Fig. 5, cross-section A, and Fig. 13). In the southern part of this structure, the deep seismicity corresponds to the eastward plunge of the high velocity body with increasing depth.

Based on three arguments, we conclude that it is worth computing the take-off angles in a 3-D model to obtain more realistic focal solutions: 1) the focal mechanism computations using FPFIT code (Reasenberg and Oppenheimer, 1985) show better statistical results. 2) The focal solutions are more coherent from one event to its neighbours (see for example E3 and E4, P13 and P17, P3 and P12). 3) We show that some 3-D mechanisms provide a better agreement between the nodal planes and the dip and strike of geological structures as described from geological studies than 1-D corresponding solutions. Field observations in the SE of the Pelvoux massif indicate that after being thrusted onto the Dauphiné zone, the western Briançonnais nappes underwent significant normal faulting, with faults being both longitudinal (N140–N170) and transverse (N40–N90) to the Alpine structures (Sue and Tricart, 1999). The focal solutions computed in this area are in agreement with these orientations. For example, the 3-D solution computed for B6 event is more coherent with a normal N170 fault dipping towards the east, than the corresponding 1-D solution, which has a strike slip component. These focal mechanisms confirm the extension of the internal Alps as observed by Sue et al. (1999).

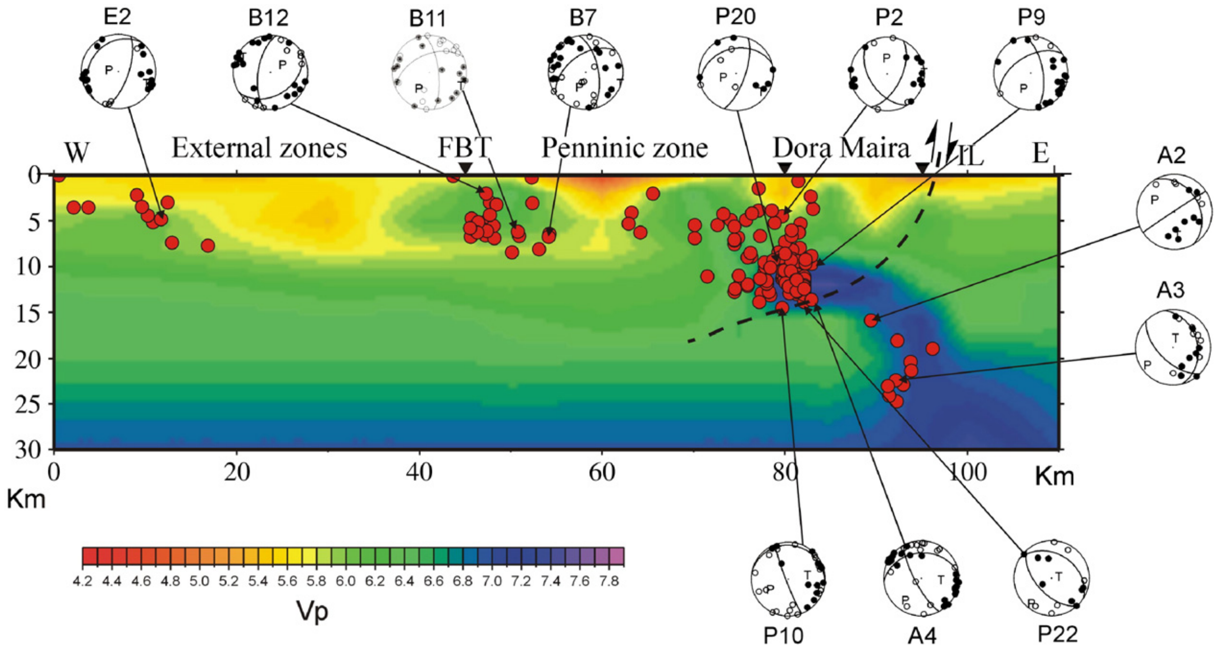

Fig. 13. Synthesis of the typical focal solutions computed in the 3-D velocity model, on an E–W depth cross-section of the Vp structure obtained with SIMULPS. The location of the cross-section is shown in Fig. 1. Hypocenters located in a 50-km wide stripe are orthogonally projected onto the section. (FBT: Frontal Briançonnais Thrust). Horizontal projections of the focal mechanisms on an inferior hemisphere are shown. The dotted line marked "IL" corresponds to the southern continuation of the Insubric Line as drawn by Schmid and Kissling (2000) on the ECORS-CROP transect.

The 3-D solutions E1, E2, E3, E4, E5 are in good agreement with the normal N–S faults mapped in this area by Labaume et al. (1989) and with the stress field obtained from the shallow seismicity by Baroux et al. (2001). The extension observed in the Briançonnais spreads in the external domain between the Pelvoux and Argentera massifs, whereas the external Alps are submitted to a transpressive tectonic regime (Thouvenot, 1996).

The most important result corresponds to the focal mechanisms computed beneath the Po basin. Fig. 13 shows a few focal solutions computed in the 3-D medium and typical of the region. In the eastern part, focal solutions are inverse in agreement with the results of Eva et al. (1997) who underline the sharp change of stress tensor orientation east of the Alpine belt. Computing focal solutions simultaneously with LET makes it possible to locate this change exactly as one crosses the postulated continuation at depth, of the Insubric line, which is already known as the outcropping boundary between European and Adriatic lithospheres in the study area. Even if field work has not shown this so far, the Insubric line thus appears to extend toward the south at depth, as a blind fault, and to play a key role in the dynamics of the south-western Alps.

4. Discussion and conclusions

It is well known that velocity models obtained by inversion of seismic travel times are not perfect, and the art of tomography is to discuss how closely they approximate the truth. As already demonstrated by Thurber (1983), Kissling (1988), Arnott and Foulger (1994) and many others, results obtained with the same code but different starting parameters or grid spacing vary around an average solution at least for well-posed problems where a unique solution exists. The use of synthetic tests generally allows to choose the best solution. One of the goals of this paper was to compare two different LET methods, in order to further check the reliability of the velocity model. In the first 20 upper kilometers, we find that the broad features of the model are stable but some variations in the locations, shapes and sizes of the anomalies are evidenced. However, these variations are of the same order of amplitude as those obtained with different inversion parameters and a single LET method. We reach similar conclusions as Haslinger and Kissling (2001) on the paraxial ray tracing. For rather long ray paths, this ray tracing yields a take-off angle of the ray at the source which can be different from the one computed with the pseudo-bending method, allowing slight improvements in the computation of focal solutions. Here, we observe instabilities in the computations of paraxial rays at depths with very sharp velocity contrasts which modify the resulting image (in the deep part of the Ivrea body) and the focal mechanisms.

We also showed that the locations of hypocenters are stable. The small shifts in depth are mainly balanced by the delay of origin times since these two parameters cannot be resolved independently.

The new focal solutions presented in this paper were obtained with a dense network, composed of permanent regional and 67 temporary stations. Paths computed with paraxial ray tracing give more reliable estimates of the take-off angle at the source, particularly in this region of very strong crustal heterogeneity. These reliable new solutions yield strong arguments on a sharp decoupling of the stress field between the shallow and western part of the Piemont units on one side and its eastern and deeper part located on the western boundary of the high velocity anomaly of the Ivrea body on the other side.

Schmid and Kissling (2000) proposed that the Ivrea body acted as a buttress during the collision of the Adriatic and European plates and that, during the early Miocene. A crustal shortening of about 60 km (along the ECORS-CROP section) was mostly accommodated by wedging, involving the European lower crust. Moreover, Pfiffner et al. (2002) calculated the effect of the Adriatic mantle wedge on a cross-section of the Central Alps and found that this wedging was important enough to bend the European lithosphere and induce the subsidence of the foreland Molasse basin. Our results deal with the present day structure and deformation near the southern termination of the Ivrea Body, thus completing towards the south the results cited above. From the structural results of our LET, one interpretative and extrapolated geological cross-section has been proposed for this southern termination of western Alps (Lardeaux et al., 2006). This one (Fig. 14) is in good agreement with the model of Cenozoic evolution of the western Alps as proposed by Schmid and Kissling (2000). However, the resolution of our local tomography limited to the upper 30 km of the crust, cannot show the present day lithospheric thickening.

One major result is the improvement of the hypocenter location recognized in the south-western Alps, respect to the geological structures and computation of reliable focal mechanisms. We show that hypocenters are closely related to the boundary between the mantle wedge of the Ivrea body and the European crust. From

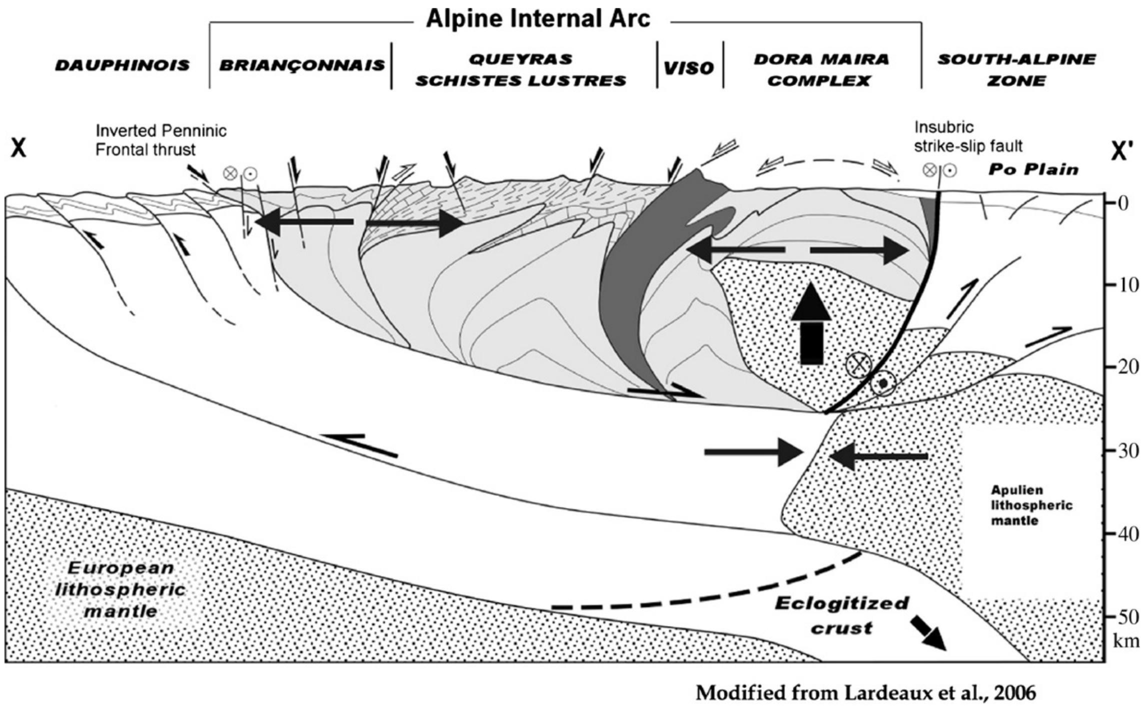

Fig. 14. Interpretative cross-section perpendicular to the main geological units and kinematics indicators, modified from Lardeaux et al. (2006). The upper part of the Apulian mantle acts as an indenter and the lower part transfers the compression onto the external arc (European foreland). In the upper crust of internal Alps an extensive regime is confirmed.

this feature, we postulate that this geological structure is still indenting the Alpine nappes stacks in the study area. The strike slip in the southern cluster (Fig. 7) and deeper transpressional events (Fig. 12) could be related to oblique NW–SE convergence along the rigid Ivrea mantle body. This is compatible with a sinistral strike slip movement between the Adriatic microplate and stable Europe, still active from 35 Ma (Ricou and Siddans, 1986; Vialon et al., 1989; Schmid and Kissling, 2000), at least in the study area. Even if field work has not shown this so far, the Insubric line appears to extend toward the south at depth, as a blind fault, and to play a key role in the dynamics of the south-western Alps, cross-cutting the Ivrea Body, thus decoupling the stress field and guiding this sinistral movement.

Acknowledgments

We thank E. Kissling and A. Pfiffner for their very fruitful comments. We also deeply thank J. M. Lardeaux for stimulating discussion and for the interpretative cross-section. The GéoFrance 3-D project (MENESR, CNRS, BRGM) supported this work. This publication is contribution 645 of UMR Géosciences Azur.

References

Arnott, S.K., Foulger, G.R., 1994. The Krafla spreading segment, Iceland; 1, Three-dimensional crustal structure and the spatial and temporal distribution of local earthquakes. J. Geophys. Res., 99, B10, 12, 23,801–23,825.

Baroux, E., Béthoux, N., Bellier, O., 2001. Analyses of the stress field in southeastern France from earthquake focal mechanisms. Geophys. J. Int. 145, 336–348.

Cattaneo, M., Augliera, P., Parolai, S., Spallarossa, D., 1999. Anomalous deep earthquakes in northwestern Italy. J. Seismol. 3, 421–435.

Deichmann, N., Bare, M., Braunmiller, J., Ballarin, D., Bay, F., Delouis, B., Fah, D., Giardini, D., Kastrup, U., Kind, F., Kradolfer, U., Kunzle, W., Rothlisber, S., Salichon, J., Sellami, S., Spuhler, E., Wiemer, S., 2000. Earthquakes in Switzerland and surrounding regions during 1999. Eclogae Geol. Helv. 93, 395–406.

Eberhart-Phillips, D., 1993. Local earthquake tomography: earthquake source regions. In: Iyer, H.M., Irahara (Eds.), Seismic Tomography: Theory and Practice. Chapman and Hall, New York, pp. 613–643.

Eva, E., Solarino, S., Eva, C., Neri, G., 1997. Stress tensor orientation derived from fault plane solutions in the southwestern Alps. J. Geophys. Res. 102 (B4), 8171–8185.

Ghose, S., Hamburger, M., Virieux, J., 1998. Three dimensional velocity structure and earthquake locations beneath the northern Tien Shan of Kyrgyzstan, central Asia. J. Geophys. Res. B2 (103), 2725–2748.

Groupe de recherche Géofrance 3-D, 1997. Géofrance 3-D: l'imagerie géologique et géophysique du sous-sol de la France. Mém. Soc. Géol. Fr. 172, 53–71.

Haslinger, F., Kissling, E., Ansorge, J., Hatzfeld, D., Papadimitriou, E., Karakostas, V., Makropoulos, K., Kahle, H.G., Peter, Y., 1999. 3-D crustal structure from local earthquake tomography around the Gulf of Arta (Ionan region, NW Greece). Tectonophysics 304 (3), 201–218.

Haslinger, F., Kissling, E., 2001. Investigating effects of 3-D ray tracing methods in local earthquake tomography. Phys. Earth Planet. Inter. 123 (2–4), 103–114.

Kissling, E., 1988. Geotomography with local earthquake data. Rev. Geophys. 26 (4), 659–698.

Kissling, E., Ellsworth, W.L., Eberhart-Phillips, D., Kradolfer, U., 1994. Initial reference models in local earthquake tomography. J. Geophys. Res. 99, 19635–19646.

Labaume, P., Ritz, J.-F., Philip, H., 1989. Recent normal faults in the southwestern Alps: their relationships with compression tectonics. C.R. Acad. Sci. Paris, Ser. II 308, 1553–1560.

Lardeaux, J.M., Schwartz, S., Tricart, P., Paul, A., Guillot, S., Béthoux, N., Masson, F., 2006. A crustal-scale cross-section of the southwestern Alps combining geophysical and geological imagery. Terra Nova 18 (6), 412–422.

Laubscher, H., 1971. The large-scale kinematics of the western Alps and the northern Apennines and its palinspastic implications. Am. J. Sci. 271, 193–226.

Le Meur, H., Virieux, J., Podvin, P., 1997. Seismic tomography of the Gulf of Corith: a comparison of methods. Ann. Geofis. XI, 1–25.

Paige, C.C., Saunders, M.A., 1982. LSQR: an algorithm for sparse linear equation and sparse least squares. ACM Trans. Math. Softw. 8, 43–71.

Paul, A., Cattaneo, M., Thouvenot, F., Spallarossa, D., Béthoux, N., Fréchet, J., 2001. A three-dimensional crustal velocity model of the south-western Alps from local earthquake tomography. J. Geophys. Res. 106, 19367–19390.

Pfiffner, O.A., Schlunegger, F., Buiter, S.J., 2002. The Swiss Alps and their peripheral foreland basin: stratigraphic response to deep crustal process. Tectonics 21 (2), 3–16.

Reasenberg, P., Oppenheimer, D., 1985. FPFIT, FPPLOT and FPPAGE: Fortran computer programs for calculating and displaying earthquake fault-plane solutions. U. S. Geol. Surv. Open-File Rep. 85–739.

Ricou, L.E.L., Siddans, A.W.B., 1986. Collision tectonics in the western Alps. In: Coward, M.P., Ries, A.C. (Eds.), Collision Tectonics. Geol. Soc. Spec. Publ., vol. 19, pp. 229–244.

Rothé, J.P., 1941. Les séismes des Alpes françaises en 1938 et la sismicité des Alpes Occidentales. Ann. Inst. Phys. Globe Strasbourg III (3), 1–105.

Schmid, S.M., Kissling, E., 2000. The arc of the western Alps in the light of geophysical data on deep crustal structure. Tectonics 19, 62–85.

Solarino, S., Kissling, E., Sellami, S., Smiriglio, G., Thouvenot, F., Granet, M., Bonjer, K., Seljiko, D., 1997. Compilation of a recent seismicity data base of the greater Alpine region from several seismological networks and preliminary 3D tomographic results. Ann. Geofis. 11, 161–174.

Sue, C., Tricart, P., 1999. Late Alpine brittle extension above the Frontal Pennine Thrust near Briançon, Western Alps. Eclogae Geol. Helv. 92 (2), 171–181.

Sue, C., Thouvenot, F., Fréchet, J., Tricart, P., 1999. Widespread extension in the core of the western Alps revealed by earthquake analysis. J. Geophys. Res. 104, 25611–25622.

Tapponnier, P., 1977. Evolution tectonique du systéme alpin en Mediterranee: poinçonnement et écrasement rigide-plastique. Bull. Soc. Geol. Fr., 7, XIX, 3, 437–460.

Thouvenotn, F.,1996. Aspects géophysiques et structuraux des Alpes occidentales et de trois orogènes: Atlas, Pyrénées, Oural, Thesis Univ. J. Fourier, Grenoble, France.

Thurber, C.H., 1983. Earthquake locations and three-dimensional crustal structure in the Coyote Lake area, central California. J. Geophys. Res. 88, 8226–8236.
Thurber, C.H., 1993. Local earthquake tomography: velocity and Vp/Vs-theory. In: Iyer, H.M., Irahara (Eds.), Seismic Tomography: Theory and Practice. Chapman and Hall, New York, pp. 563–583.
Um, J., Thurber, C.H., 1987. A fast algorithm for two-point seismic ray tracing. Bull. Seismol. Soc. Am. 77, 972–986.
Vialon, P., Rochette, P., Ménard, G., 1989. Indentation and rotation in the western Alpine arc. Alp. Tectonics 45, 329–338.
Virieux, J., 1991. Fast and accurate ray tracing by Hamiltonian perturbation. J. Geophys. Res. 96, 579–594.
Virieux, J., Farra, V., Madariaga, R., 1988. Ray tracing in laterally heterogeneous media for earthquake location. J. Geophys. Res. 93, 6585–6599.